

Fatigue Behavior of the Al-5wt%Si-2.5wt%Cu alloy produced by Combining Grain Refining Techniques: Electromagnetic Stirring with Al-5wt%Ti-1wt%B

Wendel L. Beil^{a*} , Gabriela L. Brollo^b, Cristiano Cardoso^c, Eugênio J. Zoqui^b 

^aInstituto Federal de Educação, Ciência e Tecnologia de São Paulo (IFSP), R. Primeiro de Maio, 500, 08571-050, Itaquaquecetuba, SP, Brasil.

^bServiço Nacional de Aprendizagem Industrial (SENAI), São Paulo, SP, Brasil.

^cUniversidade Estadual de Campinas (UNICAMP), Faculdade de Engenharia Mecânica, R. Mendeleyev, 200, 13083-860, Campinas, SP, Brasil.

Received: January 20, 2023; Revised: September 25, 2023; Accepted: November 24, 2023

This article studies the fatigue behavior of the Al-5wt%Si-2.5wt%Cu alloy. The effect of combining techniques of chemical grain refining (Al-5wt%Ti-1wt%B alloy) added to electromagnetic stirring, CGR+EMS, is demonstrated in this work. This combination produced a microstructure with reduced grain size ($121 \pm 20 \mu\text{m}$) when compared with the raw material produced only by electromagnetic stirring, EMS, ($213 \pm 38 \mu\text{m}$), with grain refiner Only, CGR, ($184 \pm 23 \mu\text{m}$) or Without any Grain Refining Technique (WGRT) ($413 \pm 96 \mu\text{m}$). The condition produced by associating electromagnetic stirring with the Al-5wt%Ti-1wt%B grain refiner presented the smallest grain size and less porosity. Thus, conditions CGR+EMS and WGRT were chosen to continue the evaluation of the mechanical performance of the studied alloy via tensile tests, whose results for ultimate tensile stress, yield strength and elongation were, respectively, WGRT/ CGR+EMS, UTS = $160.3 \pm 9.5 / 208 \pm 10 \text{ MPa}$, YS (0.2%) = $110 \pm 2 / 135 \pm 3.5 \text{ MPa}$ and $\epsilon(\%) = 3.2 \pm 0.1 / 2.9 \pm 0.1$. Fatigue tests were conducted via the staircase method. The average estimate of fatigue strength for a given life (10^7 cycles) and the standard deviation calculated for WGRT and CGR+EMS condition were, respectively, $\hat{\mu}_y = 60.1 \text{ MPa} / 71.6 \text{ MPa}$ and $\hat{\sigma}_y = 3.30 / 6.42$.

Keywords: *fatigue, staircase method, grain refining, electromagnetic stirring.*

1. Introduction

According to Dieter¹, 80% of in-service failures are due to fatigue. Mechanical systems parts are constantly being stressed cyclically. Such cyclic stresses lead to microscopic physical damage to the metals being stressed. Alternation of these stresses, well below the yield strength of the metal, allows the microscopic damages to become macroscopic, initiating cracks that evolve and lead to catastrophic failure of the mechanical part. The transition from microscopic to macroscopic damage and then to failure is called fatigue². Fatigue failure is influenced by environmental factors, cycling frequency, residual stresses on the surface and microstructure. Fatigue resistance is generally increased in metals as the size of inclusions, voids and grain size is reduced without decreasing the ductility of the material². Thus, in general, fatigue resistance decreases as the grains grow³. However, studies carried out with the aluminum alloy 2423-T3 show that grains measuring between 50 and $100 \mu\text{m}$, at the Paris stage, resulted in higher resistance to fatigue crack propagation and lower fatigue crack growth rate when compared to grains below $50 \mu\text{m}$. The crack path was more tortuous in the alloy with grains ranging from 50 to $100 \mu\text{m}$ when compared to grains smaller than $50 \mu\text{m}$ and larger than $355.2 \mu\text{m}$. The increase in fatigue resistance for grains ranging from 50 to $100 \mu\text{m}$ could be attributed to deflections in the crack, grain boundary interaction and plasticity induced by crack closure⁴.

Grain refining in aluminum alloys has been explored to promote improvements in grain size⁵ and microstructure morphology⁶, thus leading to an improvement in the mechanical performance of these alloys. During metal solidification, grain refining can be achieved in three different ways: by rapid cooling induced by high solidification rates⁷ (restriction of grain growth); by different modes, such as electromagnetic stirring⁸⁻¹⁰, mechanical stirring⁷, or ultrasonic vibration (grain breakage)¹¹; adding chemical grain refiners, such as the mother alloy Al-5wt%Ti-1wt%B¹² and with the addition of rare earth Er, all reported in the literature^{13,14} (nucleation stimulation). In this work, grain refining is achieved with the simultaneous use of chemical refining (CGR), with the Al-5wt%Ti-1wt%B alloy, and electromagnetic stirring (EMS). The alloy's refining potential is increased by this combination because stirring is more efficient when acting in the presence of solid nuclei, either formed on the mold walls (which are at $20 \text{ }^\circ\text{C}$) or by the chemical grain refiner. This study will present the microstructures of all the conditions used to produce the raw material, showing grain refining efficiency with the combination of CGR+EMS refining techniques. However, only the mechanical properties of the alloy produced without any technique (WGRT) and with the combination of techniques (CGR+EMS) will be presented, as well as its average estimate of fatigue resistance evaluated by the staircase method.

*e-mail: wendelleme@ifsp.edu.br

2. Materials and Methods

To produce the alloy studied in this work, an ingot mold made of copper alloy was used in all trials. The mold cooling gallery has a water flow of 40 l/min, which conditioned the mold walls at 20 ± 2 °C. Both mold and ingot produced are shown in Figure 1.

The ingots were produced from the 356 alloy and commercially pure Al and Cu, in four refinement conditions: (a) without any grain refining technique (WGRT), (b) only submitted to electromagnetic stirring (EMS), (c) with chemical grain refining only (CGR) and, finally, (d) with simultaneous application of chemical refiner and electromagnetic stirring (CGR + EMS). The magnetic field used for electromagnetic stirring varied between 12 (center) and 25 Gauss (periphery). This measurement was carried out at room temperature. The alloy Al-5wt%Ti-1wt%B, at 0.2% content, was used when chemical grain refinement was applied.

Optical microscopy with brightfield technique was used to obtain black and white (B&W) micrographs and with polarized light to obtain color micrographs. The colored micrographs allows the grain size measurements with the same precision as the electron backscatter diffraction (EBSD) technique¹⁵ that made the use of the intercept method of Hein for grain size calculation according to ASTM E112-2013¹⁶, possible. A magnification of 50x, the smallest amplitude allowed by the microscope, was applied so that at least 50 grains were intercepted by straight lines in the same field of view in the micrograph. In the condition in which no refining technique was used, sequential images were obtained at 50x magnification and later assembled so that the condition of 50 intercepted grains per field of view was met. B&W micrographs were used to quantify pores in %area via the ImageJ software. To quantify the pores, 9 micrographs were used at 50x magnification, thus, a central strip of 2x18 mm was scanned in the analysis.

The tensile tests were performed according to ASTM E8-E8M-21¹⁷, using a MTS universal testing machine, model 810. Fatigue tests followed the criteria established by ISO 12107-12(E)¹⁸ and were carried out in a TQ TecQuipment model SM1090 rotary flex fatigue testing machine. The tests were conducted at room temperature, with a frequency of 60 Hz and subjected to a load ratio $R = -1$, alternating completely. The fatigue specimens were produced according to ISO 1143-2010(E)¹⁹ via turning. The adopted roughness of $R_z = 6.77 \pm 0.47$ μm (result from the turning operation) is the typical roughness of machining in general, being found in gearbox unions faces, housings of bearings²⁰. The fracture surfaces were examined using a ZEISS EVO MA 15e scanning electron microscope from the Multiuser Laboratory for Materials Characterization from DEMM/FEM/UNICAMP.

3. Results and Discussion

3.1. Raw material, grain size and porosities

The chemical composition of the ingots produced in this work was measured with an ANACON BILL OES optical emission spectrometer. The result is presented in Table 1.

Figure 2 shows colored (a to d) micrographs of the studied alloy cast using different techniques. Figure 3 B&W micrographs show the alloy's dendritic structure that is progressively refined with the use of refining techniques (a, c e e), presenting the most refined structure when the combined techniques are applied (g). As can be seen, it is impossible to measure the crystalline grains with B&W metallography, given the impossibility of reliably locating grain boundary regions, due to the difficulty in distinguishing whether the neighboring entities separated by eutectic are distinct grains or only dendritic arms belonging to the same grain.

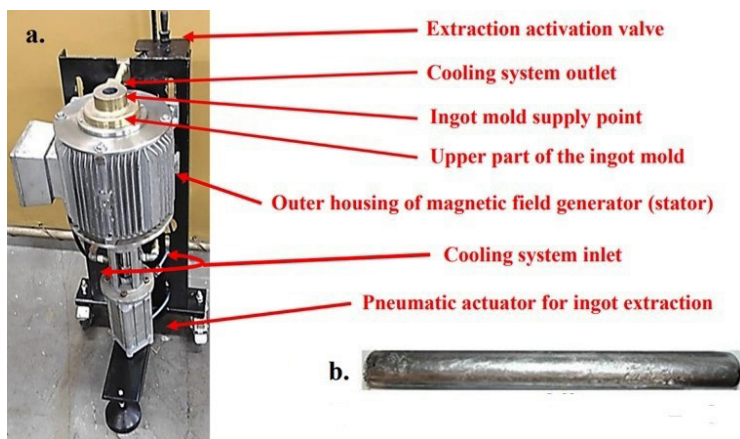


Figure 1. a. Ingot Mold; b. Example of ingot produced.

Table 1. Chemical composition of the Al-5Si-2.5Cu alloy in wt.%.

Si	Cu	Mg	Fe	Mn	Ti	Al
4.98 ± 0.17	2.49 ± 0.13	0.18 ± 0.02	0.24 ± 0.03	0.07 ± 0.0	0.27 ± 0.03	Bal.

Using the images obtained by polarized light, Figure 2a to d, it is possible to distinguish different grains and measure the evolution of the grain refinement sought in this work. Figure 2a shows the large extent that a grain can occupy when no refining technique is adopted. Under this condition, grains can reach more than 1 mm in length. Expressive grain refining can already be observed when isolated refining techniques are adopted (b and c). Finally, the association of techniques (d) potentialized grain refinement, since the electromagnetic stirring (provided by the action of the Lorentz force) is more efficient in the presence of multiple solid nuclei formed by both the contact of the liquid bath with the mold walls (where the magnetic field is more intense), and largely by the grain refiner that is a strong nucleation agent. These nuclei and/or fragments are continuously pulled out and taken to the center of the bath being used as more nucleation sites for new grains.

Figures 3a-h show too examples of porosities, highlighted in red for the Imagej software analysis. Porosities were found in the alloy produced under all conditions and are called generically pores. These pores are composed of shrinkage voids and gas porosities. The geometry of the discontinuities can be observed in Figures 3a-h. The numbers associated with the arrows represent the circularity values for the respective pores. The distinction between shrinkage and gas porosity

was attributed to the geometry of the pore. Studies performed with micro-CT observed that low sphericity is associated with shrinkage and higher sphericity indexes are related to gas porosity²¹. Porosity studies performed in parts manufactured via the high pressure die casting process (HPDC) show that sphericity values lower than 0.4 were related to shrinkage while higher values were related to porosities originating from gas²². It can be seen in Figures 3a-h that in all conditions of production of raw material, in micrographs taken from the center of the ingots, there is the presence of porosities with irregular contours. The pores present irregular boundaries molding themselves to the dendritic branches adjacent to them and with very low circularity indexes (up to 0.05), as can be seen in Figure 3d. Irregular pores are formed due to the ingot's radial solidification inside the mold. The solidification front evolves from the inner face of the mold, where the heat exchange for cooling the ingot takes place, to the center of the ingot, leading to the occurrence of shrinkages. Such porosities occur in the final moments of solidification due to the metal contraction and limited or inadequate supply of liquid^{23,24}.

Shrinkage pores are characterized by molding themselves to the boundaries of neighboring dendritic arms and, then, present a low roundness index. Also, these pores are formed at the center of the ingot, due to the aspects of radial solidification mentioned before.

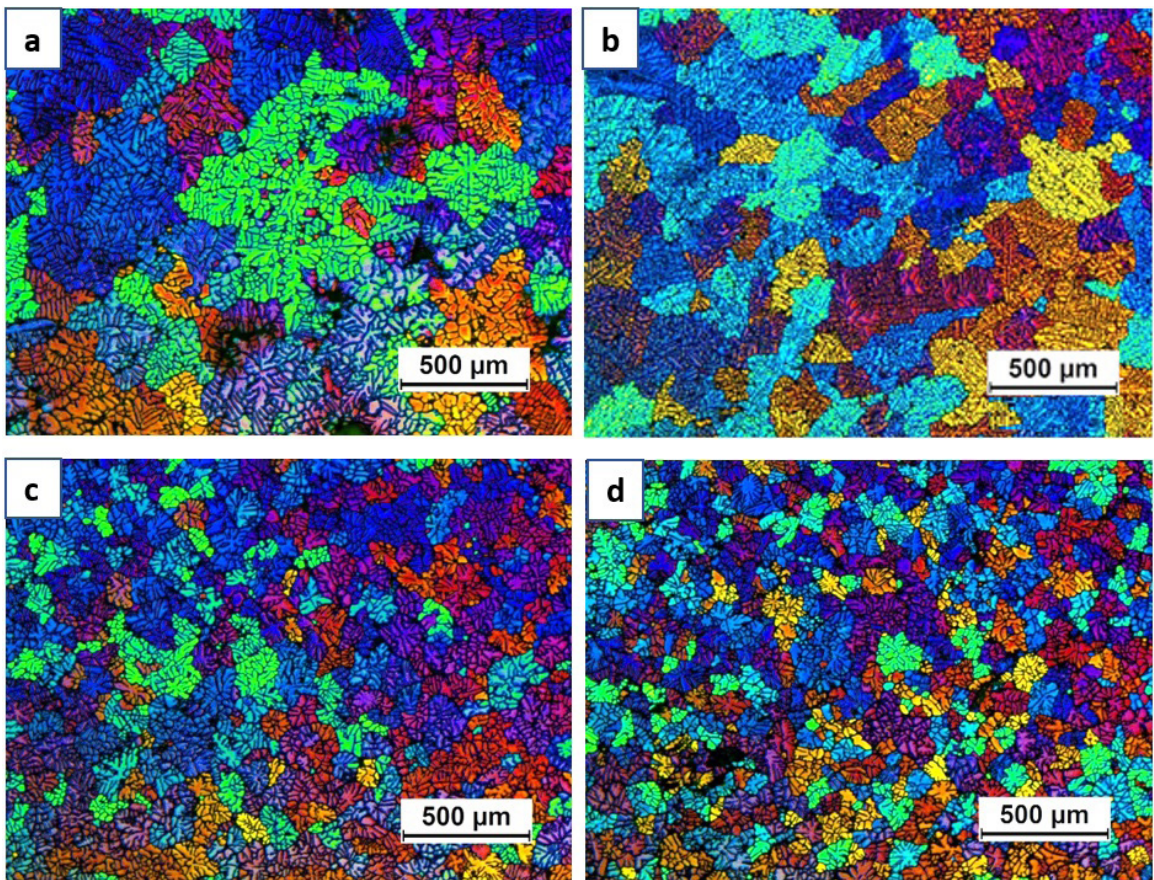


Figure 2. Colored micrographs showing the studied alloy cast under different conditions: a. without the grain refining techniques (WGRT); b. electromagnetic stirring (EMS) only; c. chemical grain refining (CGR) only; d. chemical refining and electromagnetic stirring (CGR + EMS).

Figures 3a, 3b and 3c, 3d show that, in conditions WGRT and CGR, in addition to the presence of porosities whose circularities are very low, there are multiple points widely distributed throughout the micrograph. These points are often located within the Al- α phase with sphericity indices between 0.5 and 0.85 and reaching up to 1.0 (fully circular). The occurrence of multiple porosity points is more pronounced for the CGR condition. Characteristically, porosities form in the last stages of the solidification process²⁵. With the progress of the solidification, these porosities have to adjust to the remaining spaces in the eutectic, left by the dendritic branches. Thus, if the grains are reduced, the spacing is also reduced and consequently porosities are smaller. Figure 4 shows the action of the different refining techniques discussed on both

grain size (gray) and porosity média (red). For the alloy WGRT condition, a grain size of $414 \pm 96 \mu\text{m}$ is achieved. On the other extreme, when the two refining techniques are combined (CGR + EMS), the grain size drops to $121 \pm 20 \mu\text{m}$. Not only a significant reduction in grain size (342%) occurs, but also a more homogeneous microstructure, given that the standard deviation for grain size dropped by 480%. In addition, under the conditions where EMS was used, not only the absolute % of porosities are smaller but also the distribution of the pores is more homogeneous along the microstructure (see Figure 3a-h) this effect of EMS on the pores has already been reported in previous works²⁶. It can be seen that a decrease in the percentage of porosities occurs only in the conditions in which EMS was used (Figure 4).

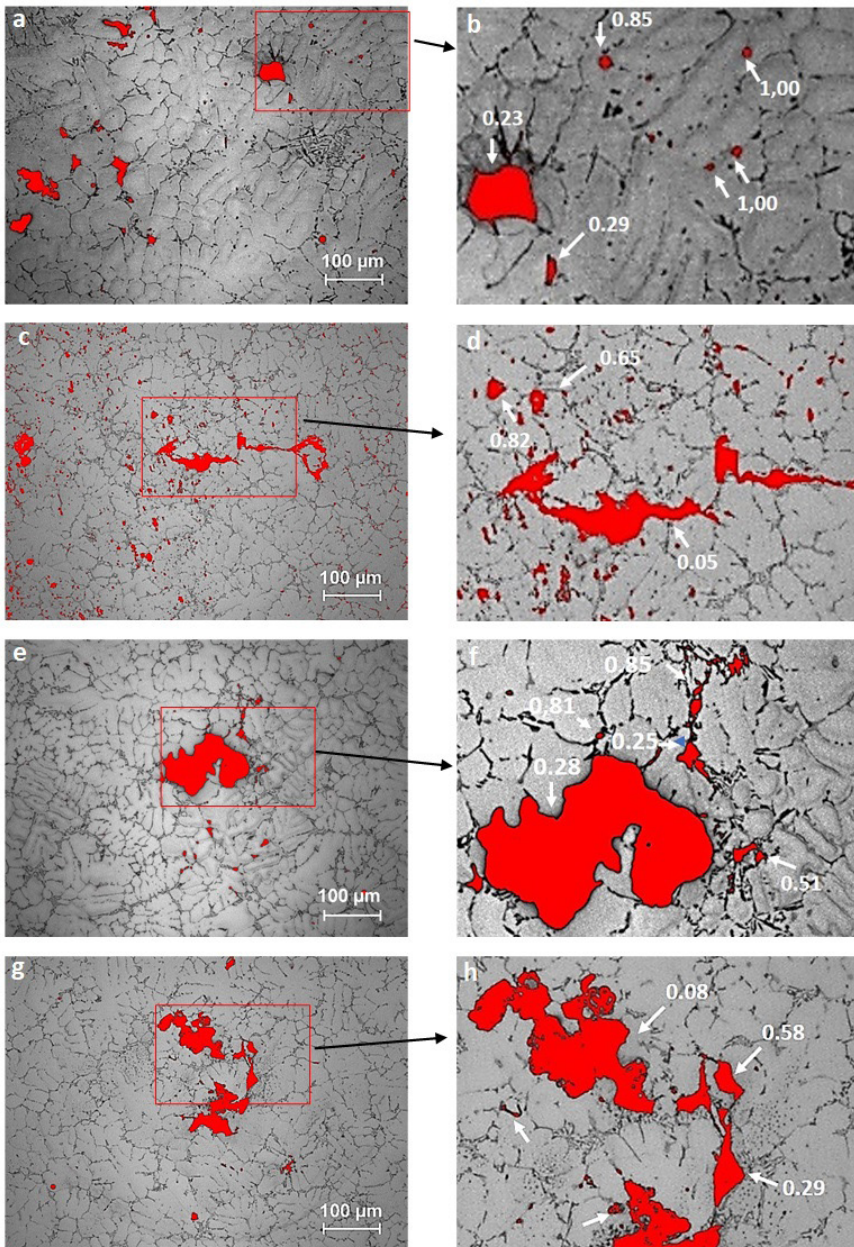


Figure 3. Micrographs B&W showing the studied alloy cast under different conditions: a, b. WGRT; c, d. chemical grain refining (CGR) only e, f. electromagnetic stirring (EMS) only; g, h. CGR+EMS.

Figure 5 shows this behavior under the conditions in which EMS and CGR+EMS were used: the decrease in porosity frequencies occurred in the porosities whose roundness values are above 0.5 (gas porosities). This effect kept the count fixed at values with circularity around 0.5, suggesting an association of these porosities with circularity of 0.5 and

below (shrinkages), since they are observed in all conditions. It can be seen in Figure 3 that, even with the decrease in grain size provided by the CGR, the percentage of pores remains practically unchanged when compared to the WGRT condition. However, in the CGR condition (Figure 5), an increase in the frequency of porosities it can be seen with circularity close to and greater than 0.5, which are typical values of smaller porosities (micrographs shown in Figures 3c and 3d).

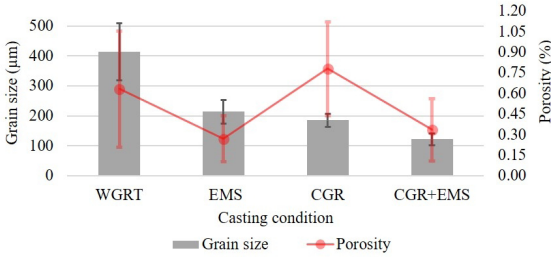


Figure 4. Grain size and porosity for all the tested refining conditions.

3.2. Fatigue and mechanical properties.

Fatigue tests, tensile tests and hardness tests were carried out only in the conditions that represent the largest and smallest grain sizes and percentage of porosities. Figure 6 shows the order of events that occurred during the fatigue tests for both conditions, WGRT and CGR+EMS. The first stress value to be used must be the closest to the fatigue strength limit of the material¹⁸. Since the studied alloy does not exist in the literature, the initial stress of 58 MPa and 68MPa were adopted in this work, respectively for the WGRT and CGR+EMS conditions.

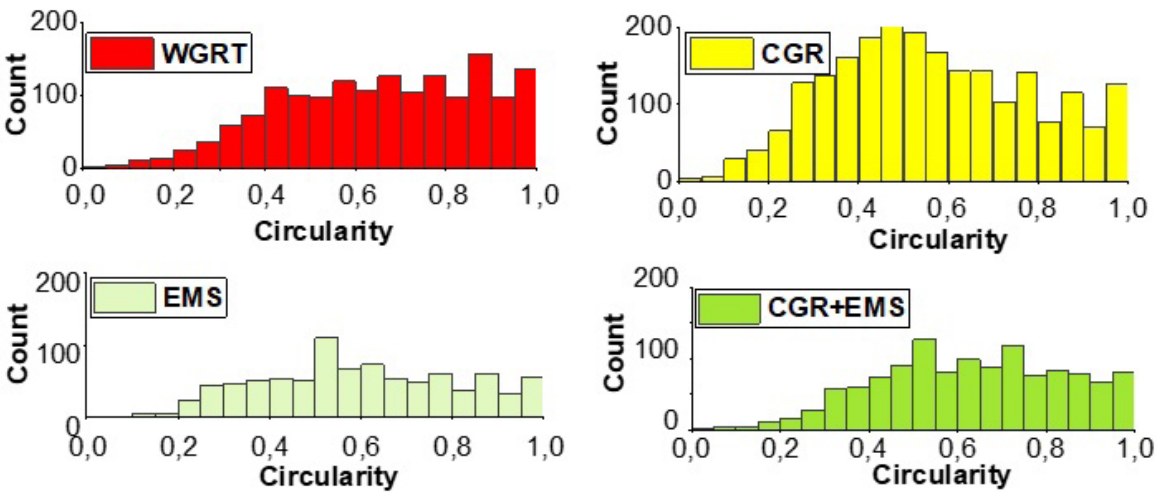


Figure 5. Histograms showing the observed frequencies for the conditions: WGRT, EMS, CGR and CGR+EMS.

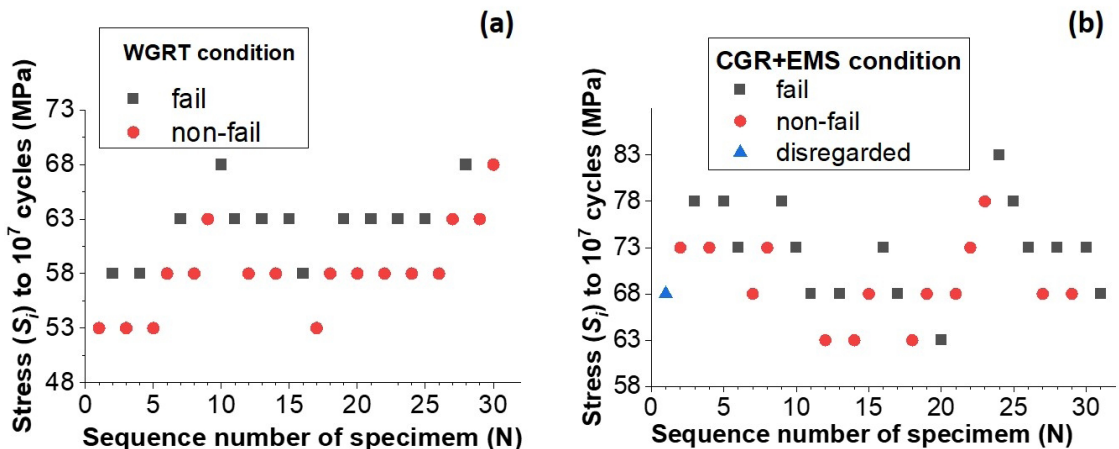


Figure 6. Sequence of events during the fatigue tests of the (a) WGRT and (b) CGR+EMS conditions.

The chosen value is based on the endurance limits of the 319.0 as cast alloy: 76 MPa (sand casting) and 83 MPa (permanent mold casting), considering that the fatigue endurance limit is smaller for machined samples from cast parts in relation to as cast test bars²⁷. The chosen value is reasonable, since only one specimen was disregarded in the tests. Concerning the choice of the fixed value of 5 MPa used for addition (if the event is non-fail at 10^7 cycles) or subtraction (if the event occurred is a failure in values smaller than 10^7 cycles), it was also shown to be assertive and to have met the criterion that the fixed value of the step must satisfy the condition $0.5\sigma < d < 2\sigma$, since the equations used to estimate the fatigue life are based on this criterion²⁸. This fixed value was based on the work carried out by Fachinni, whose initial process for raw material production was similar to what was used here, although for an alloy with lower Si content²⁹. The values of $D=0.409$ and $D = 0.739$ for the conditions WGRT and CGR+EMS also meet the established criterion that $D > 0.3$ ¹⁸. Based on stress levels (S_0, S_1 , and S_2) and (S_0, S_1, S_2 , and S_3), shown in Table 2 and Table 3, the number of degrees achieved were 6 and 9, which leads to the coefficients $k_{(10,95)} = 2.755$ and $k_{(10,95)} = 2.355$ for a failure probability of 10% and a reliability level of 95%¹⁸, for the WGRT and CGR+EMS conditions, respectively¹⁸. Based on the values obtained in the events that occurred and using the equations indicated in the standard, the following is calculated: the average estimate of fatigue strength $\hat{\mu}_y$ for a given fatigue life (10^7 cycles), the standard deviation $\hat{\sigma}_y$, and the lower fatigue strength limit \hat{y} ($k, 10, 95$)(18).

The values obtained in the fatigue, tensile and hardness tests and the relationships between fatigue and other properties are presented in Table 4.

The results from the tensile tests did not show expressive changes in elongation for the different grain sizes tested. However, the ultimate tensile stress and yield strength increased as grain size and porosity decreased. Yield strength is larger for more refined grains, showing an inverse relationship. Such behavior can be attributed to the larger number of existing grain boundaries in refined grains that serve as obstacles to dislocation movements, resulting in higher values of strength³⁰. Hardness values were practically the same for both tested conditions.

The indexes achieved from the $\hat{\mu}_y / YS$ and $\hat{\mu}_y / UTS$ ratios were very close for both conditions, suggesting that tensile tests can be used to reference the first values for fatigue tests.

3.3. Fractography

Figure 7 shows the path taken by the fracture in the two conditions tested under fatigue. The arrows indicate the crack propagation direction, pores and the catastrophic failure region. Figure 7a (WGRT condition) shows a higher pore concentration and larger pores when compared to the CGR+EMS condition. Note that in Figures 7a and 7b the paths taken in both conditions are composed of two distinct regions, one of initial and crack propagation and the other of catastrophic failure. However, in Figure 8a the path taken until reaching the catastrophic failure region is practically straight, presenting a tortuosity only in the catastrophic failure region.

Table 2. Organization of failed events of WGRT condition according to standard 12107:2012(E).

Stress (MPa)	i	f_i	if_i	$i^2 f_i$
$S_2 = 68$	2	2	4	8
$S_1 = 63$	1	7	7	7
$S_0 = 58$	0	3	0	0
Sum	-	C=12	A=11	B=15

Table 3. Organization of non-failed events of CGR+EMS condition according to standard 12107:2012(E).

Stress (MPa)	i	f_i	if_i	$i^2 f_i$
$S_3 = 78$	3	1	3	9
$S_2 = 73$	2	4	8	16
$S_1 = 68$	1	6	6	6
$S_0 = 63$	0	3	0	0
Sum	-	C=14	A=17	B=31

Table 4. Estimated mean fatigue life ($\hat{\mu}_y$), standard deviation ($\hat{\sigma}_y$), lowest fatigue strength limit (\hat{y}), ultimate tensile stress (UTS), yield strength (YS), elongation (ε) and the relationship between $HB / \hat{\mu}_y, \hat{\mu}_y / YS, \hat{\mu}_y / UTS$ for the Al-5wt%Si-2.5wt%Cu alloy.

	$\hat{\mu}_y$ (MPa)	$\hat{\sigma}_y$ (MPa)	\hat{y} (MPa)	UTS (MPa)	YS (MPa)	E (%)	HB (125kgf/5 mm)	$HB / \hat{\mu}_y$	$\hat{\mu}_y / YS$	$\hat{\mu}_y / UTS$
WGRT	60.1	3.55	50.29	160.3 ± 9.5	110 ± 2.0	3.2 ± 0.1	59.6 ± 6.3	0.99	0.54	0.37
CGR+EMS	71.6	6.2	56.7	208 ± 10.6	135 ± 3.2	3 ± 0.1	59.8 ± 5.9	0.82	0.52	0.34

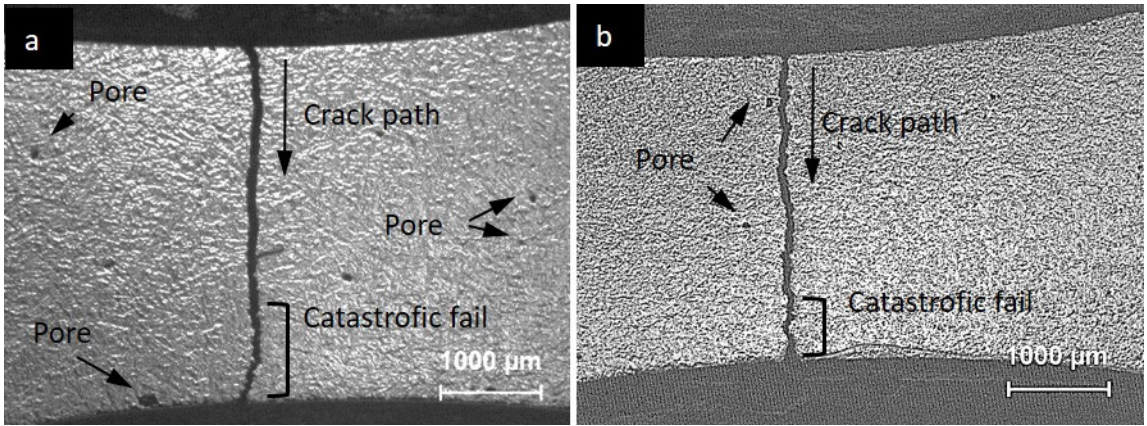


Figure 7. Fracture path shown in the: a) WGRT condition; b) EMS+CR condition.

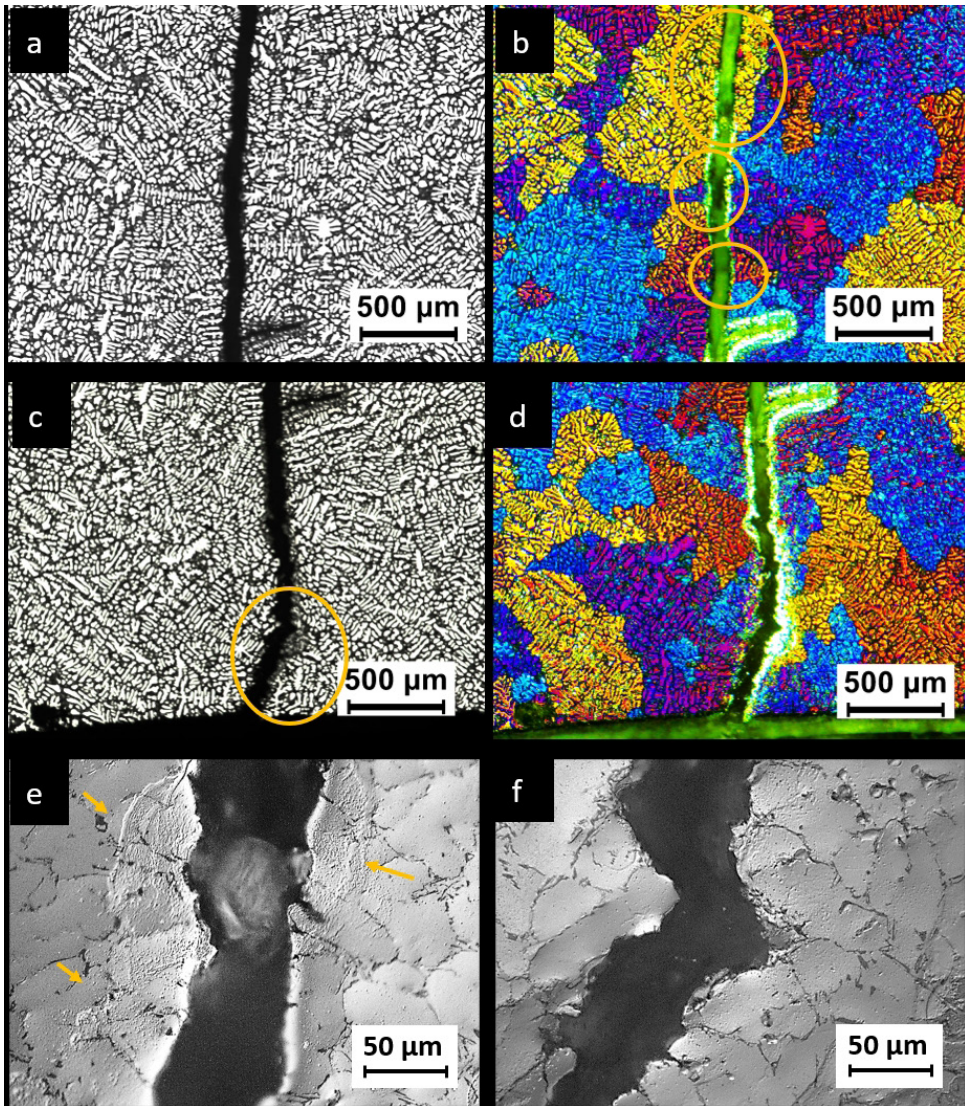


Figure 8. Micrographs from the WGRT condition showing: a) B&W micrograph of the path taken by the crack in the propagation region and b) corresponding colored micrograph; c) B&W micrograph of the path taken by the crack in the region of catastrophic failure, and d) corresponding colored micrograph e) enlarged detail showing plastic deformation in the crack propagation region and f) enlarged detail showing intergranular fracture in the catastrophic failure region.

This feature is evidenced in Figure 8a, which presents a slightly sinuous path and in Figure 8c, at the final section, presenting a tortuosity which does not allow us to define the three stages of fatigue fracture. In the WGRT condition samples, the crack propagation occurred in a straight line, characterizing a transgranular fracture, since the driving force for the propagation of the transgranular crack is smaller. This can be seen in the colored micrograph at the regions indicated in Figure 8b, which allows the visualization of grains of the same color that passed through the crack and accompanied by plastic deformation as observed in Figure 8e. Figure 7b (CGR+EMS condition) shows a tortuous crack path throughout its length, which can also be seen in an enlarged image in Figures 9a and 9c, different from the crack path shown in 8a and 8c. This difference in the trajectory of the paths taken

by the cracks is attributed to the different grain sizes observed in the conditions studied here, since the grains with dimensions $121 \pm 20 \mu\text{m}$ (CGR+EMS condition) have a higher fraction of grain boundaries than grains with $413 \pm 96 \mu\text{m}$ (WGRT condition). Smaller grains constitute more resistant obstacles to crack growth because the crack will follow the path with the lowest driving force necessary to propagate. Grains sizing of $121 \pm 20 \mu\text{m}$ result in a more tortuous path taken by the crack and a larger expenditure of energy and, consequently, a higher fatigue resistance. Crack propagation for samples in the CGR+EMS condition, the fracture alternation between intergranular and transgranular can be observed by following the crack path in Figure 9, with fragments of grains of the same color and of different colors on the opposite fracture boundaries. Plastic deformation can also be seen in Figure 9e.

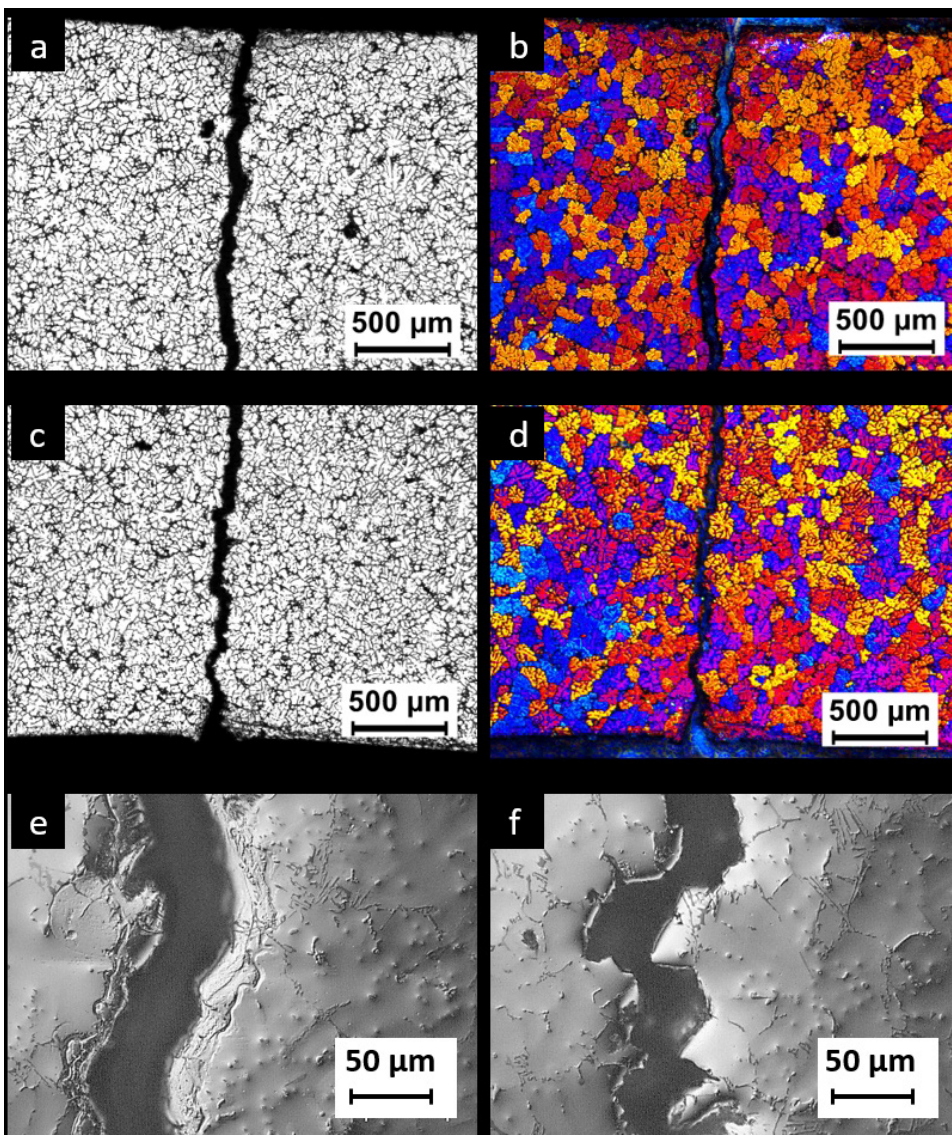


Figure 9. Micrographs from the CGR+EMS condition showing: a) B&W micrograph of the path taken by the crack in the propagation region and b) corresponding colored micrograph; c) B&W micrograph of the path taken by the crack in the catastrophic failure region and d) corresponding colored micrograph; e) enlarged detail showing plastic deformation in the crack propagation region and f) enlarged detail showing intergranular fracture in the catastrophic failure region.

In the regions of catastrophic failure, both conditions studied present a similar behavior, with the crack path traversing the grain boundaries (intergranular fracture) where the eutectic is located (figures 8d and 9d), presenting regions with little or no plastic deformation, featuring a brittle fracture (figures 8f and 9f).

Figure 10 shows the fracture surfaces with the three stages of fatigue fracture that occurred in both tested conditions. The red arrows indicate stress concentration points that originated the cracks. For the CGR+EMS condition (Figure 10a), the fracture occurred outside the neck region, with the fracture surface measuring a diameter of 4.497 mm, as shown in the profile vector in Figure 10b, whereas for the WGRT condition, the fracture surface diameter measured 4.064 mm, which is the measurement of the neck (Figure 10b). The different measurements indicate that, even with refined grains, there is a strong influence of porosities on crack nucleation: porosities act as stress concentration points and also reduce the cross section of the specimen, causing the fracture to occur outside the neck region in an apparently larger cross-section. The yellow dashed lines delimit regions that represent stage I and sometimes transition regions between stages I and II of fatigue. In these regions, a smoother and flat surface can be seen (10a and 10b). These surfaces are represented in the graphs of surface profiles (Figure 10c, 10d and 10e), where the straight segments that pass through the regions delimited by the yellow dashed lines show a low variation of the amplitude in the graphs, qualitatively representing smoother and higher variations in rougher regions, with smoother regions (of low amplitude) associated with stage I of fatigue³⁰. Regarding the other stages of fatigue II and III, macroscopically it is possible to make only a few observations. In the case of Figure 10, the CGR+EMS condition, patterns of practically straight lines are observed, indicated by sequential arrows.

Stage I fatigue usually begins at some point on the surface where a stress concentration occurs. Some metallurgical aspects directly influence the occurrence of crack initiation, such as: shape, distribution and size of porosities³¹⁻³³, oxide films, silicon particles and iron-rich phases^{34,35}. Works carried out under the studied conditions indicate the presence of casting defects, porosities and shrinkage in all cases of crack initiation (Figure 11 and Figure 12a, 12b and 12c). At the WGRT condition, it is observed, along with the casting surface defects, the presence of silicon particles in Figure 12a, iron-rich phase in Figure 12c, whose stoichiometry suggests the β -Fe phase and copper-rich phase suggesting Al_2Cu . In all conditions indicated as crack initiation points, SEM-EDS analysis was performed, whose analysis points are indicated in Figure 11 and Figure 12 while results are expressed in Table 5.

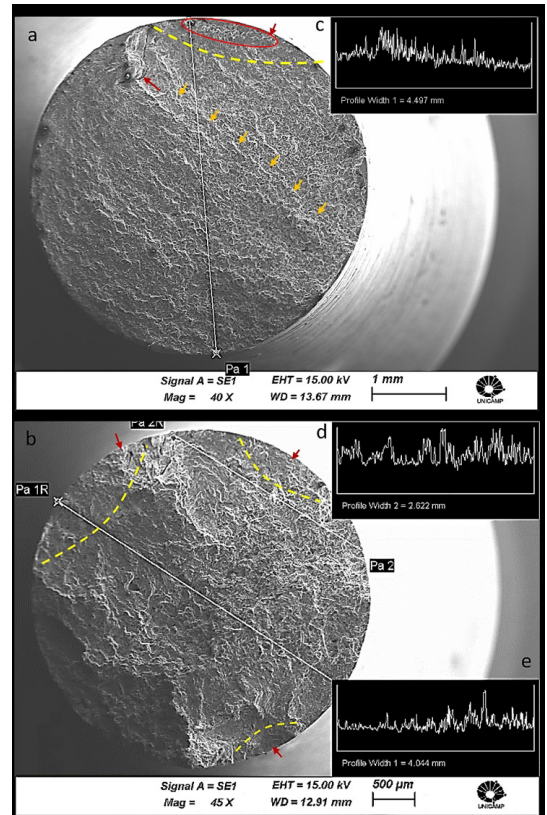


Figure 10. Images of fatigue fracture surfaces in: a) sample produced in the CGR+EMS condition and in b) sample produced in the WGRT condition.

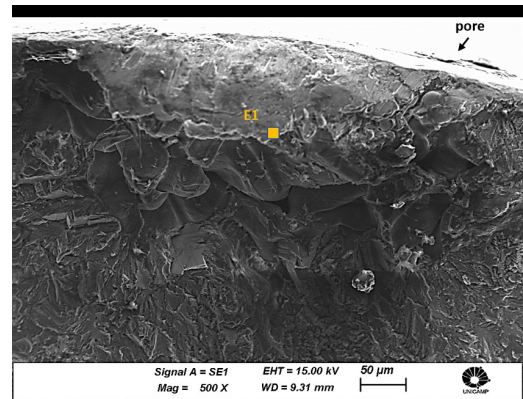


Figure 11. Crack initiation point occurred in the sample in the CGR+EMS condition.

Table 5. Punctual chemical analysis performed by SEM-EDS in Figures 11 and 12.

Suggested phases	Espectrum	Elements (weight %)						
		Mg	Al	Si	Ti	Fe	Cu	Total
α -Al	E1	0	96.77	1.74	0.28	0	1.21	100
Eutético (AlSi) θ - Al_2Cu	E2	3.07	67.9	25.55	0	0	3.41	100
Eutético (AlSi) θ - Al_2Cu	E3	0	91.89	5.68	0	0	2.43	100
β - Al_3FeSi	E4	0	43.29	43.66	0	13.05	0	100

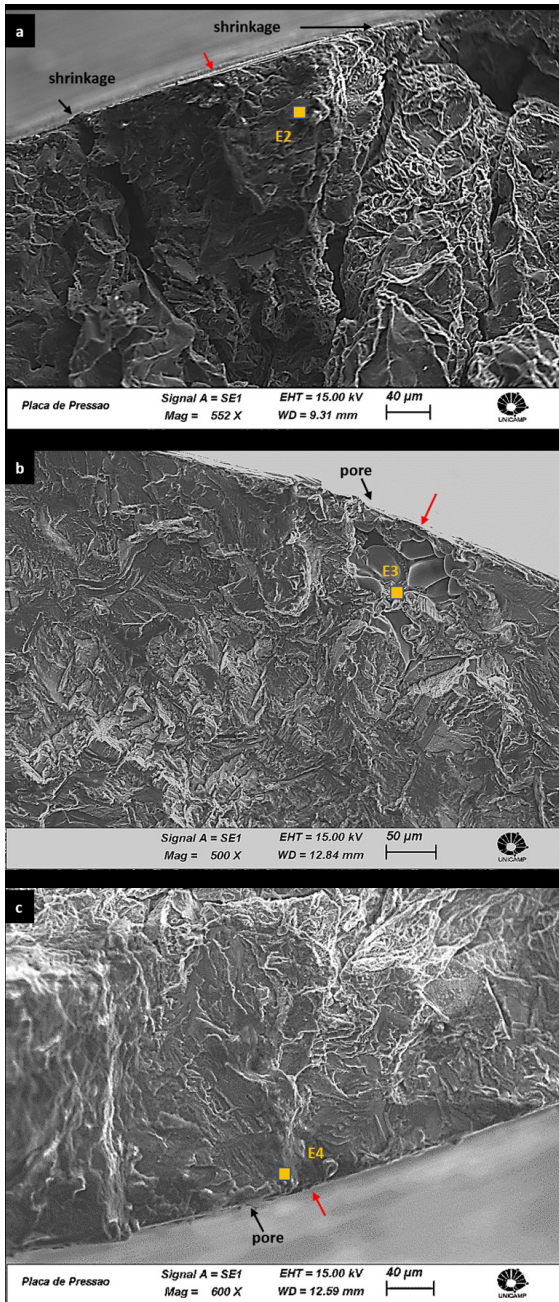


Figure 12. Multiple crack initiation points shown in a), b) and c) in the WGRT condition.

Figures 13a and 13b represent the fracture surface in stage II, showing the presence of striations in both conditions, characterizing the fracture as a result of fatigue. The striations are shown to be irregular, following different orientations, and sometimes appearing as microcracks. This appearance is attributed to a transgranular fracture, which confirms the hypothesis raised in Figures 8b and 9b. In Figure 14, the CGR+EMS condition shows the presence of striations in the observation plane and in depth (showing up in steps), being more expressive in the CGR+EMS condition when compared to the WCRT condition.

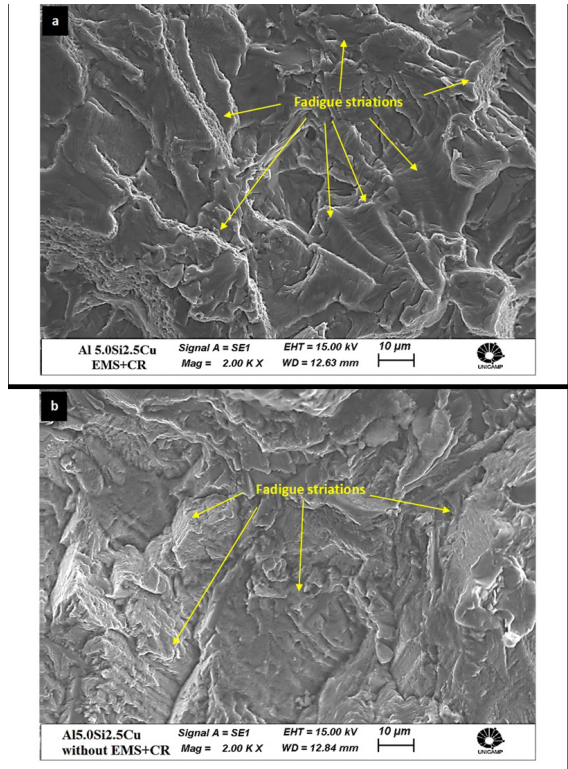


Figure 13. Images showing stage II fatigue in: a) CGR+EMS condition and b) WGRT condition.

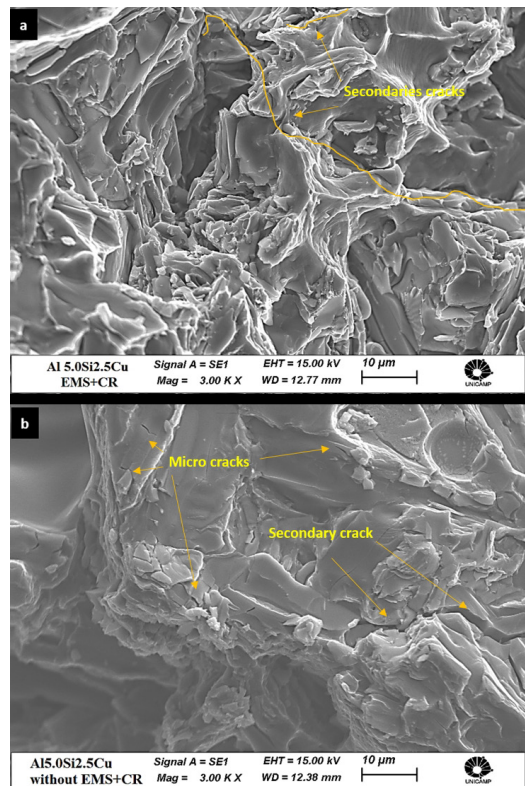


Figure 14. Images showing stage III fatigue in: a) CGR+EMS condition and b) WGRT condition.

Figures 14a and 14b show the fracture surfaces in stage III. Stage III consists of the last phase of fatigue crack propagation, when the cross section of the specimen no longer supports the applied load, leading to an overload causing sudden failure³⁶. The fracture surfaces are rough showing eutectic components for both conditions. Secondary cracking and microcracking can be seen. Both the cracks and the eutectic components are more evident in the WGRT condition, which presents larger grains, silicon particles and larger precipitates when compared to the CGR+EMS condition. Preferably, the fracture occurred transgranularly, in accordance with the images in Figure 8 and Figure 9.

4. Conclusions

The combination of techniques CGR+EMS using these parameters are an efficient route for producing Al-Si-Cu alloys with a refined microstructure. Results can be summarized seen below:

- The reduction in grain size of 342% was achieved as well as a more homogeneous microstructure, given that the standard deviation for grain size dropped by 480%. In addition to contributing to grain refining, electromagnetic stirring is efficient in reducing gas porosity.
- The samples in the CGR+EMS condition, with grains measuring $121 \pm 20 \mu\text{m}$, showed the best results in fatigue resistance for the life of 10^7 cycles (i.e., 71.6 MPa), as well as the best results for ultimate tensile stress and yield strength, when compared to the WGRT samples, which presented grains measuring $413 \pm 96 \mu\text{m}$ and a fatigue resistance of 60.1 MPa.
- Fracture analyses show that the CGR+EMS condition presented a tortuous fracture path, showing the influence of grain boundaries on crack propagation when compared to the WGRT condition, which presented a smoother and straighter crack path, in addition to presenting multiple points of crack nucleation as a result of the higher percentage of porosities presented.
- The tests carried out enabled the estimation of the fatigue life for the alloy Al-5wt%Si-2.5wt%Cu, 71.6 MPa, using specimens with the surface finish of $R_z = 6.77 \pm 0.45$, conventional finish of turning and conventional machining processes in general, such as those performed on mechanical components such as gear box joint faces and bearing housings. This surface finish is considerably inferior to that used in usual fatigue tests, leading to more realistic results concerning the fatigue performance of the alloy. The tests also permitted the establishment of relationships between the estimated fatigue life and the yield strength, estimated fatigue life and ultimate tensile stress and between the Brinell hardness and the yield strength for the alloy, which are a reference for choosing the initial test stress, to carry out future tests based on previous tensile tests.

5. Acknowledgments

The authors would like to thank the Metalúrgica Itapira company, the Federal Institute of Science and Technology Education of São Paulo, IFSP (campus Itaquaquecetuba), the SENAI Institute for Innovation in Advanced Manufacturing and Micro Manufacturing and the UNICAMP School of Mechanical Engineering for the practical support provided. This work was carried out with the support of Fapesp (Process 2018/11802-4).

6. References

1. Dieter GE. *Metalurgia mecânica*. 2ª ed. Rio de Janeiro: Guanabara Koogan; 1981.
2. Dowling N. *Mechanical behavior of materials: engineering analysis applied to deformation, fracture and fatigue*. 4th ed. London: Pearson; 2018.
3. Turnbull A, de los Rios ER. The effect of grain size on fatigue crack growth in an aluminium magnesium alloy. *Fatigue Fract Eng Mater Struct*. 1985;18(11):1355-66.
4. Shou WB, Yi DQ, Liu HQ, Tang C, Shen FH, Wang B. Effect of grain size on the fatigue crack growth behavior of 2524-T3 aluminum Alloy. *Arch Civ Mech Eng*. 2016;16(3):304-12.
5. Naruccci CN Jr, Antunes AS, Abdalla Ajguan R, Tie D. Effect of the heterogeneous nucleation of the primary α -Al grain via the Al-4Nb-0.5B master alloy in Al-Si alloys with high Fe content. *Mater Res*. 2021;24(4):e20200544.
6. Guan R, Tie D. A review on grain refinement of aluminum alloys: progresses, challenges and prospects. *Acta Metall Sin*. 2017;30(5):409-32.
7. Zimpel I, Bartex SLT, Barcellos VK. Effects of stirring time and cooling rate on the rheocast microstructure and mechanical properties of magnesium alloy MRI 230D. *Mater Res*. 2021;24(3):e20200482.
8. Beil WL, Brollo GL, Zoqui EJ. Continuous casting device with electromagnetic stirring for production of SSM feedstock using Al-Si alloys. *Mater Res*. 2021;24(3):e20200584.
9. Mikolajczak P. Microstructural evolution in AlMgSi alloys during solidification under electromagnetic stirring. *Metals*. 2017;7(3):89.
10. Mikolajczak P. Effect of rotating magnetic field on microstructure in AlCuSi alloys. *Metals*. 2021;11(11):1804.
11. Dobatkin VI, Eskin GI. Ingots of aluminium alternative the semi solid alloys with nondendritic structure produced by ultrasonic treatment for deformation. In: 4th International Conference on Semi-solid Processing of Alloys and Composites; 1996; Sheffield. Proceedings. Sheffield: University of Sheffield; 1996. p. 193-6.
12. Osório WR, Peixoto LC, Garcia A. Efeitos da agitação mecânica e de adição de refinador de grão na microestrutura e propriedade mecânica de fundidos da liga Al-Sn. *Materia*. 2009;14(3):906-17.
13. Kord S, Siadati MH, Alipour M, Amiri H, Koppad PG, Gowda AC. Microstructure and mechanical behaviour of as cast and hot extruded AlZnMgCu alloy with rare earth erbium additions. *Iran J Mater Sci Eng*. 2018;15:62-9.
14. Kord S, Alipour M, Siadati MH, Kord M, Koppad PG. Effects of rare earth Er additions on microstructure and mechanical properties of the Al-Zn-Mg-Cu Alloy. In: International Symposium on Light Metals; 2018; Phoenix. Proceedings. Cham: Springer; 2018. p. 441-9.
15. Nafisi S, Roccisano A, Ghomashchi R, Vander Voort G. A comparison between anodizing and EBSD techniques for primary particle size measurement. *Metals*. 2019;9(5):488.
16. ASTM: American Society for Testing and Materials. ASTM E112-2013: standard test methods for determining average grain size. West Conshohocken: ASTM; 2013.

17. ASTM: American Society for Testing and Materials. ASTM E8-E8M-21: standard test methods for tension testing of metallic materials. West Conshohocken: ASTM; 2021.
18. ISO: International Organization for Standardization. ISO 12107:2012(E) – metallic materials – fatigue testing–statistical planning and analysis of data. Geneva: ISO.
19. ISO: International Organization for Standardization. ISO 1143-2010(E) – metallic materials – rotating bar bending fatigue testing. Geneva: ISO.
20. Agostinho OL, Rodrigues ACS, Lirani J. Tolerâncias, ajustes, desvios e análise de dimensões: princípios de engenharia de fabricação mecânicas. São Paulo: Edgard Blucher; 2014.
21. Savelli S, Buffière JY, Fougerès R. Pore characterization in a model cast aluminum alloy and its quantitative relation to fatigue life studied by synchrotron X-Ray microtomography. *Mater Sci Forum*. 2000;331(337):197-202.
22. Zhang Y, Lordan E, Dou K, Wang S, Fan Z. Influence of porosity characteristics on the variability in mechanical properties of high pressure die casting (HPDC) AlSi7MgMn alloys. *J Manuf Process*. 2020;56:500-9.
23. Samuel A, Zedan Y, Doty H, Songmene V, Samuel FH. A review study on the main sources of porosity in Al-Si cast alloys. *Adv Mater Sci Eng*. 2021;2021:1-16.
24. Ammar HR, Samuel AM, Samuel FH. Porosity and the fatigue behaviour of hypoeutectic and hypereutectic Aluminum-silicon casting alloys. *Int J Fatigue*. 2008;(30):1024-35.
25. Monroe R. Porosity in casting. Schaumburg: American Foundry Society; 2005. p. 1-28. (05-2456(4)).
26. Guo A, Zhao J, Xu C, Li H, Han J, Zhang X. Effects of pouring temperature and electromagnetic stirring on porosity and mechanical properties of A357 aluminum Alloy rheo-diecasting. *J Mater Eng Perform*. 2018;27(5):2373-80.
27. Kaulfman JG, Rooy EL. Aluminum Alloy castings. Materials Park: ASM International; 2004.
28. Dixon WJ, Mood AM. A method for obtaining and analyzing sensitivity data. *J Am Stat Assoc*. 1948;43(241):109-26.
29. Fachinni CA, Gregolin A, Zoqui EJ. Effect of T6 heat treatment on the mechanical behavior of thixo-forged Al3Si2.5Cu alloy. In: 10th Brazilian Congress of Manufacturing Engineering; 2019; São Carlos. Proceedings. Rio de Janeiro: ABCM; 2019.
30. Nah JJ, Kang HG, Huh MY, Engler O. Effect of strain states during cold rolling on the recrystallized grain size in an aluminum alloy. *Scr Mater*. 2008;58(6):500-3.
31. González-Velásquez JL. Fractography and failure analysis. Cham: Springer; 2018.
32. Yang Z, Kang J, Wilkinson DS. The effect of porosity on fatigue of die cast AM60. *Metall Mater Trans, A Phys Metall Mater Sci*. 2016;47(7):3464-72.
33. Kuchariková L, Tilová E, Uhrčík M, Belan J. Porosity formation and fatigue properties of AlSiCu cast alloy. *MATEC Conf*. 2018;157:07003.
34. Kuchariková L, Medvecká D, Tillová E, Belan J, Kritikos M, Chalupová M, et al. The effect of the β -Al5FeSi phases on microstructure, mechanical and fatigue properties in A356.0 cast alloys with higher Fe content without additional alloying of Mn. *Materials*. 2021;14(8):1943.
35. Yi JZ, Gao YX, Lee PD, Lindley TC. Effect of Fe-content on fatigue crack initiation and propagation in a cast aluminum–silicon alloy (A356–T6). *Mater Sci Eng A*. 2004;386(1-2):396-407.
36. Campbell FC. Elements of metallurgy and engineering alloys. Materials Park: ASM International; 2008.